DISCOVERY OF ROTATIONAL MODULATIONS IN THE PLANETARY-MASS COMPANION 2M1207b: INTERMEDIATE ROTATION PERIOD AND HETEROGENEOUS CLOUDS IN A LOW GRAVITY ATMOSPHERE

YIFAN ZHOU[1], DÁNIEL APAI[1,2,3], GLENN H SCHNEIDER[1], MARK S. MARLEY[4], AND ADAM P. SHOWMAN[2]
[1] Department of Astronomy/Steward Observatory, The University of Arizona, 933 N. Cherry Ave., Tucson, AZ, 85721, USA; yifzhou@email.arizona.edu
[2] Department of Planetary Science/Lunar and Planetary Laboratory, The University of Arizona, 1640 E. University Blvd., Tucson, AZ 85718, USA
[3] Earths in Other Solar Systems Team, NASA Nexus for Exoplanet System Science, USA
[4] NASA Ames Research Center, Naval Air Station, Moffett Field, Mountain View, CA 94035, USA

ABSTRACT

Rotational modulations of brown dwarfs have recently provided powerful constraints on the properties of ultra-cool atmospheres, including longitudinal and vertical cloud structures and cloud evolution. Furthermore, periodic light curves directly probe the rotational periods of ultra-cool objects. We present here, for the first time, time-resolved high-precision photometric measurements of a planetary-mass companion, 2M1207b. We observed the binary system with *Hubble Space Telescope*/Wide Field Camera 3 in two bands and with two spacecraft roll angles. Using point-spread function-based photometry, we reach a nearly photon-noise limited accuracy for both the primary and the secondary. While the primary is consistent with a flat light curve, the secondary shows modulations that are clearly detected in the combined light curve as well as in different subsets of the data. The amplitudes are 1.36% in the F125W and 0.78% in the F160W filters, respectively. By fitting sine waves to the light curves, we find a consistent period of $10.7^{+1.2}_{-0.6}$ hr and similar phases in both bands. The J- and H-band amplitude ratio of 2M1207b is very similar to a field brown dwarf that has identical spectral type but different J–H color. Importantly, our study also measures, for the first time, the rotation period for a directly imaged extra-solar planetary-mass companion.

Key words: brown dwarfs – planets and satellites: atmospheres – planets and satellites: individual (2M1207b) – techniques: photometric

Supporting material: machine-readable tables

1. INTRODUCTION

Presence of condensate clouds is one the most unique features of the ultra-cool atmosphere of directly imaged exoplanets and brown dwarfs. Studies of formation and properties of condensate clouds (e.g., Ackerman & Marley 2001; Burrows et al. 2006; Helling et al. 2008; Allard et al. 2012) have made great progress on the cloud behaviors across different spectral types, especially the role that clouds play in the *L–T* transition (e.g., Burrows et al. 2006; Marley et al. 2010). Surface gravity is suggested to be the second key parameters in defining cloud structures (e.g., Marley et al. 2012) after effective temperature. Low surface gravity objects (e.g., HR8799 bcd, Marois et al. (2008), 2M1207b, Chauvin et al. (2004)) are significantly redder and under-luminous compared to field brown dwarfs. The anomalous color and luminosity of low surface gravity objects support models including unusually thick clouds (Currie et al. 2011; Madhusudhan et al. 2011; Skemer et al. 2011, 2012). However, due to lack of observational constraint, the dependence of cloud properties on surface gravity is not very well modeled.

Intensity modulations introduced by heterogeneous clouds can be directly observed and studied via time resolved observation and rotational mapping (e.g., Buenzli et al. 2012, 2015; Radigan et al. 2012; Apai et al. 2013; Burgasser et al. 2013; Biller et al. 2015; Heinze et al. 2015; Metchev et al. 2015; Yang et al. 2015). These techniques isolate the effect of cloud properties and obtained great success in determining the rotation period and unveiling the structures of the atmospheres of brown dwarfs. Kostov & Apai (2013) demonstrated that these techniques can be applied to directly

imaged exoplanets, too, allowing comparative studies of objects with different surface gravities. However, high contrast amplifies the challenges for directly imaged exoplanets and planetary-mass companions to acquire high-precision light curves compared to isolated brown dwarfs.

2M1207b Chauvin et al. (2004) is the first directly imaged extra-solar planetary-mass companion. Chauvin et al. (2005a) and Song et al. (2006) confirmed that 2M1207b and its host 2M1207A form a bound, co-moving system. 2M1207A and b have an angular separation of 0.″78, which corresponds to a projected separation of 41.2 AU at a distance of 52.4 pc (e.g., Ducourant et al. 2008). Combining 2M1207b's age and near-infrared luminosity with brown dwarf cooling models (e.g., Baraffe et al. 2003), the object's mass is estimated to be 2.3–4.8 $M_{\rm Jup}$ (Barman et al. 2011). Even though a circumsub-stellar disk was discovered around 2M1207A (Sterzik et al. 2004), the high companion-to-host mass ratio and large separation argue for binary-like gravitational fragmentation formation (Lodato et al. 2005; Mohanty et al. 2007).

Early observations revealed that 2M1207b's color is much redder and its near-infrared luminosity is much lower than those of field brown dwarfs with similar spectra (e.g Mohanty et al. 2007; Barman et al. 2011; Skemer et al. 2011). 2M1207b's luminosity—as derived from near-infrared photometry—is ∼2.5 mag lower than that predicted based on its mid- to late L spectral type and effective temperature of ∼1600 K (Patience et al. 2010). Based on multi-band, near-infrared photometry, Skemer et al. (2011) argued that the apparent under-luminosity of 2M1207b could be explained by a model of a spatially heterogeneous atmosphere composed of patches

of thin and patches of unusually thick clouds. Similarly, Barman et al. (2011) argued that non-local chemical equilibrium could play an equally important role as thick clouds in defining 2M1207b's color and luminosity.

The discovery of additional planetary-mass companions with similarly red colors (e.g., AB Pic B, Chauvin et al. 2005b, HR8799bcde, Marois et al. 2008, 2010) and apparent underluminosity have highlighted 2M1207b as a template of low gravity ultra-cool atmospheres but as of now understanding the composition and structure of clouds and their gravity-dependence remained elusive.

In this *Paper* we present the first, high-contrast, high-cadence, high-precision, time-resolved *Hubble Space Telescope* (*HST*) photometric time series of 2M1207b, a directly imaged planetary-mass object. We successfully detect rotational modulation and measure the amplitudes in two bands and determine the rotational period. These observations probe the spatial heterogeneity and vertical structure of clouds in planetary mass objects for the first time.

2. OBSERVATION

We obtained direct images of the 2M1207A+b system on UT 2014 April 11 from 08:07:47 (JD 2456758.838738) to 16:53:18 (JD 2456759.203681) using *HST* and its Wide Field Camera 3 (WFC3, pixel scale = 0.130 mas/pixel, MacKenty et al. 2008) in the frame of the *HST* Program GO-13418 (PI: D. Apai). We acquired the observations in filters F125W (λ_{pivot} = 1245.9 nm, full width at half maximum (FWHM) = 301.5 nm) and F160W (λ_{pivot} 1540.52, FWHM = 287.9 nm), roughly corresponding to the J and H bands. We used the 256 × 256 pixels sub-array mode to avoid memory dumps during the observations. In order to provide a near-continuous coverage for detecting modulations we observed the 2M1207 system in 6 consecutive *HST* orbits, obtaining data with maximum cadence of 1.78 minutes over a baseline of 8 hr and 40 minutes. The observations were interrupted by 58-minute long Earth occultations every 94 minutes.

The observations applied space craft rolls each two orbits to allow roll-subtraction of the primary (e.g., Song et al. 2006). The telescope roll angles for orbit 1, 3, and 5, and those for 2, 4, and 6 differed by 25°. At the separation of 2M1207b, this angle difference corresponds to a displacement of 0″.34, or 2.75 and 2.30 resolution elements in F125W and F160W, respectively.

In each orbit, we used the visibility of 2380 s, which allowed us to take eight SPARS10 exposure sequences alternating between the F125W and F160W filter. Each sequence contained 2–3 identical exposures of 88.4 s with 10 non-destructive read-outs. The number of exposures were limited by time spent on filter switching and transferring the data from the instrument to the data processing computer. To improve sampling and reduce the risk that the core of point-spread function (PSF) is affected by bad pixels, we applied a 4-point dither pattern with differential "X/Y" offsets of 1″.375 in the detector frame, providing optimal non-integral (half pixel) step of 10.5 and 8.5 pixels in F125W and F160W, respectively. In total, we obtained 70 and 64 images in F125W and F160W, respectively.

3. DATA REDUCTION

3.1. Photometry

We started the reduction from the `flt` files produced by the WFC3's `calwfc3` pipeline. We did not opt to use `ima` files that contain all non-destructive read-outs, because they provided less information on 2M1207A, which saturated after the first few samples. The `flt` files are results of basic calibration, including dark current correction, nonlinearity correction, flat field correction, as well as up-the-ramp fit on the non-destructive read-outs. Pixels with data quality flags "bad detector pixels", "unstable response", and "bad or uncertain flat value" were masked out and excluded from further analysis as suggested by previous transit exoplanet spectroscopic observations (e.g., Berta et al. 2012; Kreidberg et al. 2014).

The major challenge of high contrast observation with WFC3/IR is the fact that the detector is significantly under-sampled. 2M1207A and b are only separated by ~6 pixels or ~5 FWHM of the PSF on the detector. When applying roll subtraction, notable artifacts are introduced by image shifting and interpolation. *Tiny Tim* PSF simulator (Krist 1995) offers a solution by providing Nyquist or better sampled PSF, but systematic errors of *Tiny Tim* PSF for WFC3 limits its ability in high precision photometry (Biretta 2014). Building on the large number of PSFs obtained in our program at two different roll angles, we followed a novel, two-step approach that uses a hybrid PSF. First, based on our observations, we derived correction maps for *Tiny Tim* that accurately described the scattered light component for the primary at the correct location on the detector. Second, we carried out a PSF-photometry using hybrid PSFs composed by *Tiny Tim* PSFs and the correction map by simultaneously minimizing the residuals from the primary and the secondary.

For both of 2 steps, we used *Tiny Tim* to calculate 10× over-sampled model PSFs based on the filters, the spectra (2M1207A: Bonnefoy et al. (2014), 2M1207b: Patience et al. (2010)), the telescope's actual focus, and the telescope jitter. We used the set of *Tiny Tim* parameters provided by Biretta (2014) to improve modeling the cold mask, diffraction spikes, and the coma. The focus parameters are interpolated to the precise time of the observations using the tabulated values provided by STScI.[5] To align the *Tiny Tim* PSF to the observed PSF of 2M1207A, we moved the over-sampled PSF on a coordinate grid (gird size = 0.001 pixel) using cubic interpolation, and searched for the position that minimizes the rms difference of the observed and the re-binned *Tiny Tim* PSF over a region centered on 2M1207A with a 5-pixel-radius aperture centered on 2M1207b excluded. Then we introduced another *Tiny Tim* PSF for 2M1207b and fit the position of 2M1207b and the scales of the *Tiny Tim* PSFs of 2M1207A and b simultaneously by minimizing the residual from both primary and secondary. In the first step, we discovered that the difference of observed PSFs and model PSFs was very stable for a specified telescope roll angle and dithering position. Therefore, at the end of the first step, we derive 8 (2 roll angles × 4 dithering positions) correction maps for each filter:

$$\mathrm{Corr} = \mathrm{Median}\left(\mathrm{PSF_{obs.}} - \mathrm{PSF_{model}}\right) \qquad (1)$$

---

where PSF$_{model}$ was a combination of two scaled *Tiny Tim* PSFs for 2M1207A and b. In the second round, we combined the correction map linearly with the two *Tiny Tim* PSFs to generate hybrid PSFs, and scaled the correction map together with the two PSFs so that the residual, which is expressed as

$$\mathrm{Residual} \;=\; \mathrm{Image} - a \times \mathrm{PSF_A} - b \times \mathrm{PSF_b} - c \times \mathrm{Corr}$$

(2)

is minimized by least square fitting. We found that by introducing the correction term, the reduced χ^2 decreased from ∼10 to ∼1. Relative photometry was acquired from the scaling parameters of the *Tiny Tim* PSFs. We demonstrate examples of the original images, images with primary substracted *Tiny Tim* PSFs, and correction maps in Figure 3.

Our final step was to correct for a slight apparent trend between the position of the targets on the detector and their fluxes. We attributed this to a combination of slight changes in the PSF profile due to pixelation and to the effect of imperfectly corrected pixel-to-pixel sensitivity variations. We corrected for the apparent position-dependent flux changes by normalizing each photometric point by the median of all fluxes measured when the target was at the same position, i.e., combining data over 6 orbits. We note that this correction was small and, as we demonstrate in the next sections, could not introduce artificial modulations that resemble the long-period variations that we identified in 2M1207b.

As our study is the first to present high-contrast, high-cadence observations, we provide a detailed analysis of the uncertainties and their impact on our results.

3.2. Uncertainty Analysis: White Noise

First we estimated the photon noise for the photometry of 2M1207b. The total photon noise of the photometry was calculated by combining the photon noise of every pixel, which was derived from count rates and detector gain. The photon noises in F125W and F160W are 1.33% and 1.02%, respectively.

Since the PSFs for the 2M1207A and b were fitted simultaneously, the uncertainties for photometry and position of the primary and secondary were coupled. Errors in position measurements of 2M1207A could potentially affect the photometry of 2M1207b. We used a Monte Carlo (MC) method to evaluate the overall systematics of the PSF fitting. We applied photometry to images that were added with random Poisson noise and repeated the photometry procedure for 1000 times. The uncertainties for F125W and F160W photometry were found to be 1.34% and 1.12%, respectively.

3.3. Uncertainty Analysis: Flat Field Uncertainties

A further contribution to photometric uncertainties may be introduced by imperfectly corrected pixel-to-pixel sensitivity differences. 2M1207b were observed at 8 different positions on the detector (2 rolls × 4 dithering positions). Imperfect flat field correction could introduce position-dependent differences in the count rates. The uncertainty of WFC3 IR flat field is typically ∼1% (Dressel 2012).

In PSF photometry, however, multiple pixels are fitted simultaneously, so that we expect the photometry to be less affected by high spatial frequency flat field noise, and have a lower than 1% uncertainty from the flat field errors. To verify

this, we multiplied every image by an artificial flat field error mask (AFEM)—a uniformly distributed Gaussian noise array with mean of 1 and sigma of 1%—and repeated the PSF photometry on the resulting images. The analysis of these experiments resulted in almost identical light curve to the original, verifying that the flat field errors did not affect our photometry significantly (Figure 2, bottom panel).

4. VERIFICATION OF PHOTOMETRIC MODULATIONS AND AMPLITUDE ESTIMATE

4.1. Tests and Verification

The light curves that resulted from our photometry showed apparently sinusoidal modulations, discussed in more detail in Section 5. To verify that these modulations are intrinsic to the object and not the result of our data reduction procedures or instrumental changes, we carried out three different tests.

First, we fitted sinusoids independently to the light curves of two filters to verify the similarity of the signal in the two bands (Figure 2, top panel) using an Markov Chain Monte Carlo (MCMC) approach (for detail see Section 4.2). Inconsistent periods or light curve shapes would argue against a genuine signal. We used sinusoids as examples of the simplest periodic functions. We found that the periods of the best fit sinusoids were similar, $11.1^{+2.0}_{-1.2}$ hr for F125W and $9.3^{+2.0}_{-0.8}$ hr for F160W. These periods are consistent within the uncertainty. Furthermore, these periods are not close to any timescales over which *HST* or WFC3 changes, and are very different from all timescales present in our observations (dithering timescales, integration times, and orbital timescales). We note that the period is close to the total time span of the observation, however, the probability that the period is equal to or less than the observation time baseline is negligible (see Section 4.2).

As a second test, we repeated the analysis neglecting the first orbit. The motivation behind this test is that, due to spacecraft thermal settling, the first orbits of *HST* observations are often slightly unstable, and are neglected in high-precision studies (e.g., Mandell et al. 2013). Indeed, in our analysis, 2M1207A is significantly fainter in the first orbit (Figure 3) than in the subsequent ones. Our analysis based on orbits 2–6 found the periods were $11.9^{+3.4}_{-1.8}$ hr for F125W and $10.7^{+4.4}_{-1.4}$ hr for F160W, which were almost identical results to our analysis using the whole 6 orbits, based on which we conclude that the first less reliable orbit does not affect our results significantly (Figure 2, middle panel).

As a third test, we explored whether a subset of images, perhaps due to imperfect normalization or correlation with specific instrument states, could drive the light curves into apparently sinusoidal shapes. To test this possibility, we split the data into two temporally overlapping halves: subset one were images taken at dithering position 1 and 3; subset two were those taken at dithering position 2 and 4. For both subsets, we repeated our analysis independently. For both of F125W and F160W, two halves demonstrated similar sinusoidal modulations. Our analysis detect sinusoidal modulations in *both* subsets and in *both* filters, with periods and amplitudes consistent with those derived from the complete data set (Figure 2, upper panel).

These tests demonstrate that the modulation seen in our data are consistently present in the different filters, in the different time segments of the data, and in data obtained in different dithering positions. All of the three tests support the signal to be intrinsic to the target.
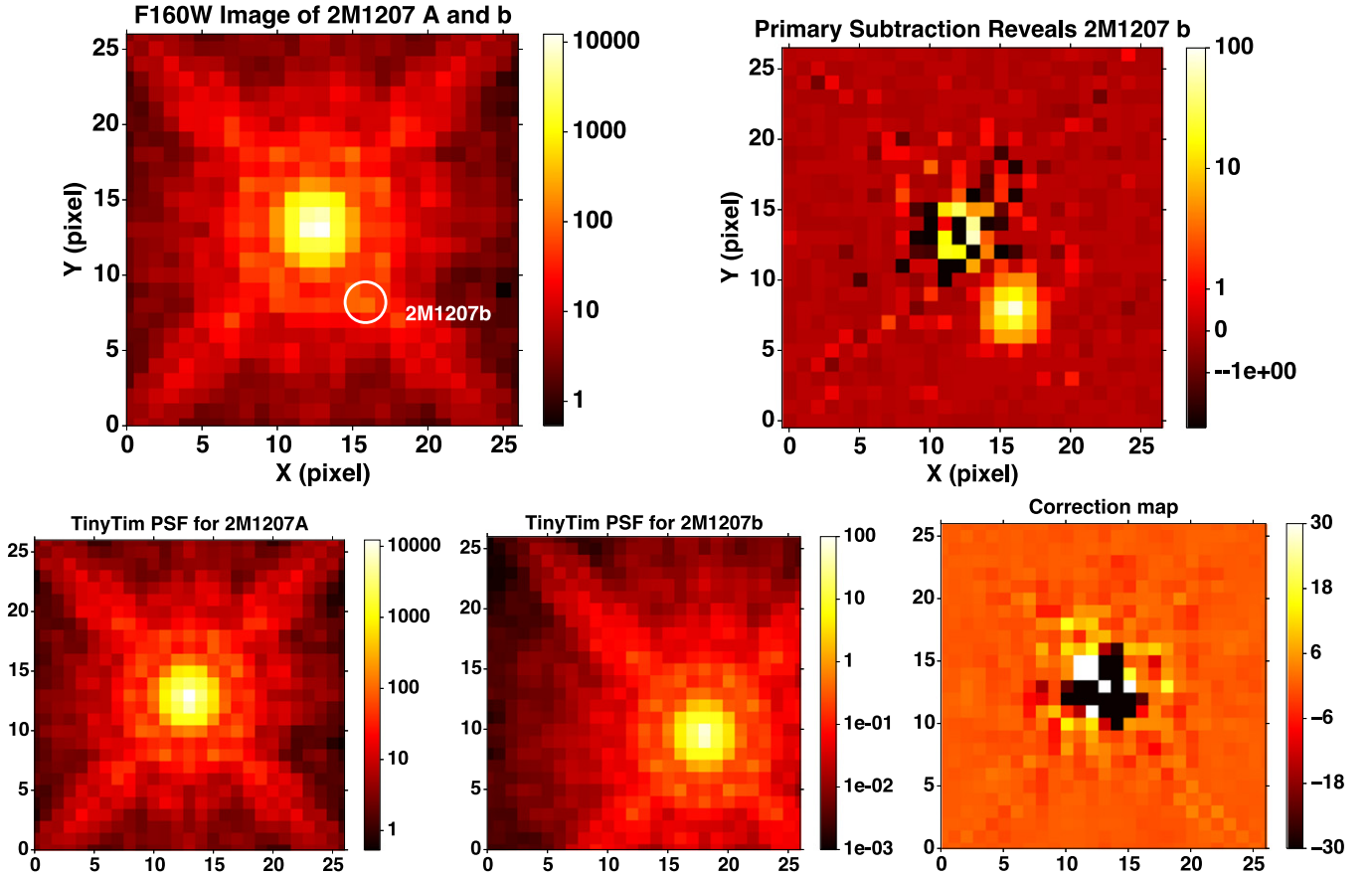
Figure 1. Point-spread function subtraction allows isolating the secondary and accurately measuring its brightness in our WFC3 F160W images. Upper row: original (left) and primary subtracted (right) images. After subtraction of the primary PSF and correction map, 2M1207b is detected at a high significance level. Lower row: examples of *Tiny Tim* PSFs for the primary and the secondary, and the correction map.

4.2. Amplitude and Period Measurements

To constrain the amplitudes and periods of the light curves, we performed sinusoidal fit using MCMC method. The priors for the amplitudes, the periods and the phases of the sine waves were all assumed to be uniform distributions. The ranges of the prior distributions were 0%–5% for the amplitudes, 2–40 hr for the periods, and 0 to 2π for the phases. The results of the MCMC fit are shown in Figure 4. The posterior distributions of the periods and amplitudes are very well constrained for both two filters so that we are able to measure the amplitudes and periods as well as their uncertainties. For F125W, the amplitude and period are $1.36 \pm 0.23\%$ and $11.1^{+2.0}_{-1.2}$ hr, respectively, and for F160W, they are $0.78 \pm 0.22\%$ and $9.3^{+2.0}_{-0.8}$ hr, respectively. Next, to place the strongest constraint on the period of 2M1207b, we jointly fitted the two light curves requiring an identical period for two filters but allowing different phases and amplitudes. The period measured from the posterior distribution of the joint fit is $10.7^{+1.2}_{-0.6}$ hr. We also repeated the fitting excluding data from the first orbit in order to quantitatively assess the influence of these less stable data points. Even in the case of limiting our data to Orbits 2–6, the posterior probability distribution peaks at periods and amplitudes very similar to those found for the entire data set, demonstrating that a periodic solution is preferred with or without the first orbit data. Nevertheless, unsurprisingly, when shortening the baseline by considering only Orbits 2–6 results in a long-period tail in the probability distribution.

To evaluate the possibility of very long period sinusoids, we integrated the posterior distributions for periods at least 2σ longer than the best fit period, as well as for periods longer than 20 hr. For the joint fit, the integrated probabilities are 12.68% longer than and 1.29% for the period longer than 13.1 (best fit + 2σ) hours and 20 hr, respectively. Given these results we conclude that periods much longer than our baseline are very unlikely.

5. RESULT

We present the first high-contrast, high-cadence, and high-precision photometry of a directly imaged planet or planetary-mass companion around another star. Our observations reveal a modulation in the light curve of the $\sim 4 M_{Jup}$ companion 2M1207b, the first detection of modulations in directly imaged planetary-mass objects. The best fit periods for F125W and F160W are $11.1^{+2.0}_{-1.2}$ and $9.3^{+2.0}_{-0.8}$ hr, respectively. Jointly fitting the two light curves gives a period measurement of $10.7^{+1.2}_{-0.6}$ hr.

We obtained high signal to noise photometry for both 2M1207A and B (Figure 3). On average, the photometric contrast is 6.52 ± 0.01 mag for F125W and 5.77 ± 0.01 mag for F160W. We provide our photometry result data in Tables 1, 2.

We find that the amplitudes in the two bands are significantly different. By fitting Gaussians to the MCMC fit result distributions, we determin that the amplitude for F125W is 1.36% with a standard deviation of 0.23%, and the amplitude
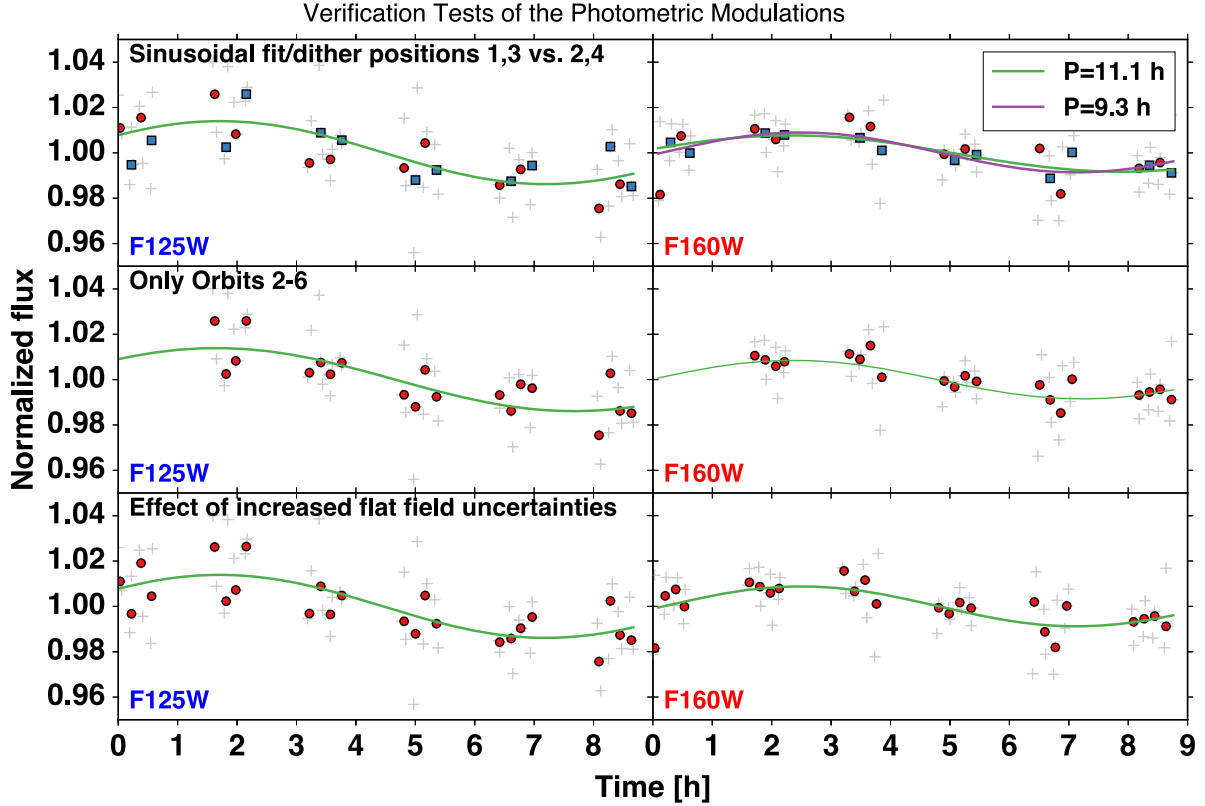
Figure 2. F125W (left) and F160W (right) light curves under different variability verification tests. Individual measurements are plotted with gray crosses. Photometric measurements of the same exposure sequence are binned, and binned photometry are plotted with points or squares. Best fitted sinusoids are plotted with solid lines. Upper: binned measurements taken in dithering position 1 and 3 (red points) and that taken in 2 and 4 (blue squares) are plotted with different symbols. The two halves of data were reduced independently, and show the same modulation trend. In upper left panel, the green line a sinusoid fitted with all parameters freely varying, and the purple line is a sinusoid fitted with the period set the same as that of F125W. Middle: sinusoids fitted without using the data taken in Orbit #1. These curves are almost identical to the curves plotted in upper panel. Lower: photometry measured with AFEM-added images and best fitted sinul curves. These points and curves are also almost identical to those plotted in the upper panel. The slight difference of normalized photometry among panels for the same filters is the result that normalization factors change when omitting the first orbit or when adding artificial noise.

for F160W is 0.78% with a standard deviation of 0.22%. The amplitudes of two bands are separated by more than 2-σ. The amplitude for F125W is 1.74 ± 0.30 times of that for F160W light curve.

6. DISCUSSION

The baseline of our observations is not long enough to cover a complete period of 2M1207b. This should come as no surprise, given the 10–20 hr long periods observed in the Solar System giant planets. Nevertheless, as the observations may cover a large fraction of the complete rotation of 2M1207b, we can derive the probability distribution of the rotation period and the amplitudes (in two bands) based on our data. To do this, we assumed an example of a simplest periodic functions, a sine wave. Approximating periodic or quasi-periodic modulations in light curves with moderate signal-to-noise with sine waves is a common approach (e.g., Buenzli et al. 2012). We used this approximation and combine it with an MCMC approach in Section 4.2 to derive posterior probability distributions.

Before discussing our MCMC results for completeness we discuss why other, non-periodic functions cannot be considered adequate fits to our data. We can exclude a flat (zero slope) lightcurve due to its poor fit (reduced $\chi^2 = 117.3/69$, $76.9/63$ for F125W and F160W, respectively). A constant, but non-zero slope line provides an improved reduced χ^2, but is not a

physically viable model: 2M1207b's time-averaged brightness cannot rapidly increase or decline. A linear decline or brightening that is not intrinsic but instrumental in nature can be excluded for three reasons: (1) the simultaneously observed 2M1207A shows no such modulation; (2) the signal is consistent between different filters and different parts of the data set; (3) all known *HST* thermal responses occur on timescales of 1 orbit or shorter (Lallo et al. 2005), inconsistent with the modulations in our data. Given that the linear models are inconsistent with our data or not physically viable, and the sine waves used in our MCMC fits provide lower reduced χ^2 than any of the linear models in both filters, we adopt those as the simplest description of the modulations. We include sine waves of period as long as 40 hr as possible solutions for our MCMC fit to consider the possibility of very long period variations. We find that a sinusoid with a period of ~ 11 hr is the most probable solution with or without including data from the first orbit. When jointly fitting F125W and F160W light curves with sinusoids with the same period but independent amplitudes and phases, the integrated posterior distributions for periods at least 2σ larger than the best fit period is 12.7%, and that for period longer than 20 hr is only 1.3%. Therefore, our observations exclude the possibility of a very long period ($p > 20$ hr) at a high confidence level. Nevertheless, the period measurement should be further constrained in the future when light curves with full phase coverage are available.
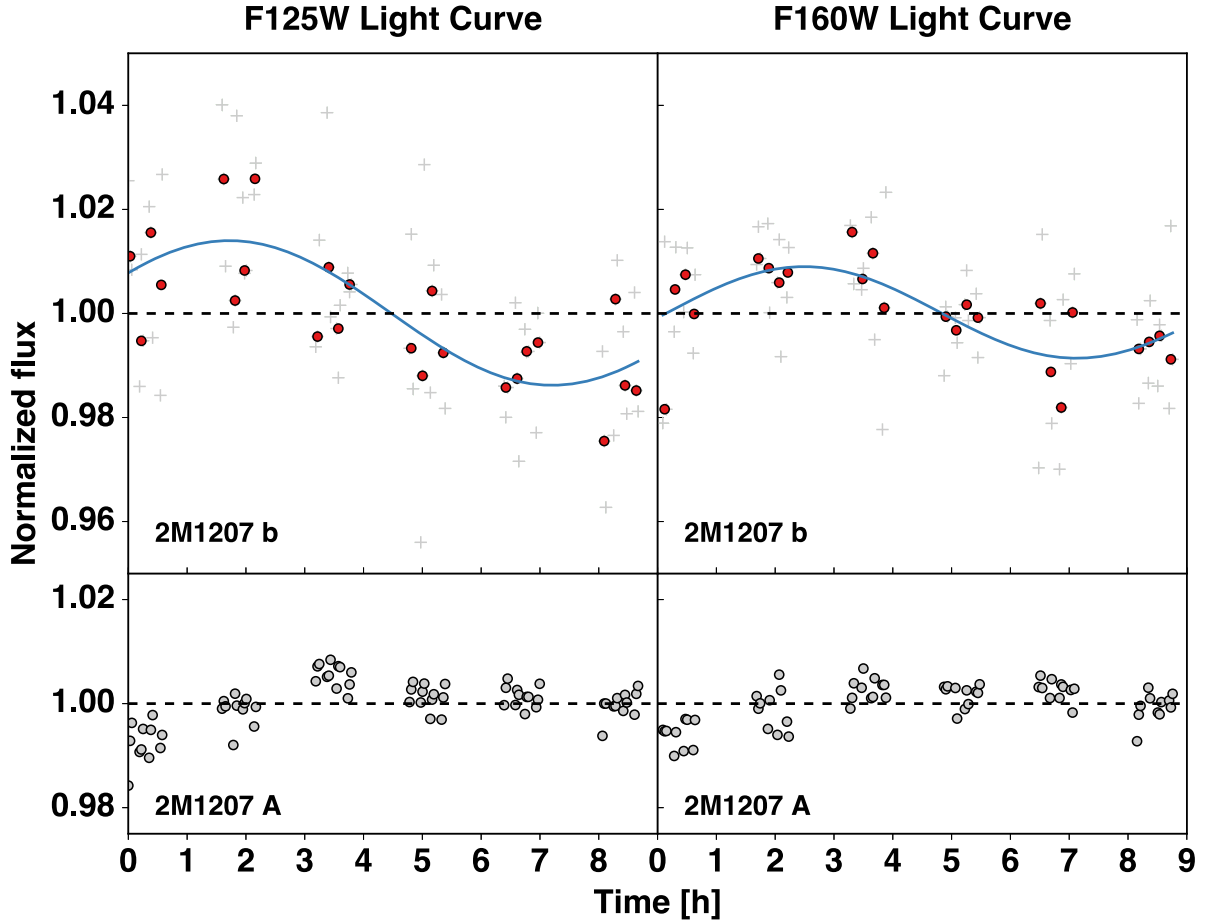
Figure 3. Normalized light curves for 2M1207B (upper) and A (lower) with filter F125W (left) and F160W (right). Unbinned measurements are plotted in gray crosses and binned photometry are plotted with red points. Best fitted sinusoids are plotted with blue solid lines.

   The direct measurement of the photometric modulation period of a directly imaged planetary-mass object is an import result of our study. We infer the rotation period of 2M1207b to be the same as the period of photometric variation. Although horizontal winds can cause the measured period to differ from true rotation period, it is unlikely that the difference is greater than the uncertainty of the measurement, since for Jupiter and Saturn, typical wind speeds are more than one order of magnitude smaller than the equatorial rotation speeds. In the left panel of Figure 5 we compare the rotation period of 2M1207b to the solar system planets, β Pic b the only other directly imaged planet with an estimated period and measured $v \sin i$, field brown dwarfs from the study of Metchev et al. (2015), and young brown dwarfs (UpSco, age $\sim$11 Myr) from Scholz et al. (2015). Snellen et al. (2014) measured $v \sin i$ for β Pic b and demonstrated that it fits a trend defined by Solar System planets in which more massive planets have faster rotation rates. The interesting finding that β Pic b, an exoplanet that formed in a protoplanetary disk, follows this trend suggests a possibly connection between planet mass, initial angular momentum, and formation in a disk.

   Excitingly, our measurement of the rotation period of 2M1207b, a planet mass companion that has similar age to β Pic b, has a rotation period that fits in the same trend, as well as majority of the brown dwarfs. As 2M1207b and β Pic b evolve and cool down, they are expected to shrink to the size of Jupiter. Order of magnitude estimation based on the

conservation of angular momentum results in final rotation periods of $\sim$5 hr and $\sim$3 hr (Snellen et al. 2014) for 2M1207b and β Pic b, respectively, which still fit to the period versus mass trend. Although 2M1207A is known to host a circumsubstellar disk (Sterzik et al. 2004), the low mass of typical brown dwarf disks (e.g., Klein et al. 2003; Mohanty et al. 2013) and its large separation argue against the possibility that 2M1207b has formed in a protoplanetary disk. The result that objects formed in different scenarios share the same trend of period versus mass suggests that rotation periods—in absence of well-determined ages—may contribute insufficient evidence for a formation in a disk versus in a cloud core environment.

   The rotation period of $\sim$10 hr is significantly longer than those of field brown dwarfs from the sample of Metchev et al. (2015), and the corresponding equatorial rotation speed ($\sim$15 km s^{-1}) is lower than most L-type field brown dwarfs (Reiners & Basri 2008). In contrast, the rotation period of 2M1207b is similar to the median period of the sample of Scholz et al. (2015), whose age is similar to 2M1207b. The rotation period of 2M1207b is within the range predicted by evolutionary track established from measurements of brown dwarfs assuming conservation of angular momentum (see Figure 4 of Scholz et al. 2015), and much longer than the break-up limit (Marley & Sengupta 2011), i.e., the rotation period where the equatorial centrifugal force exceeds gravitational force. Observed rotation rates for brown dwarfs of show
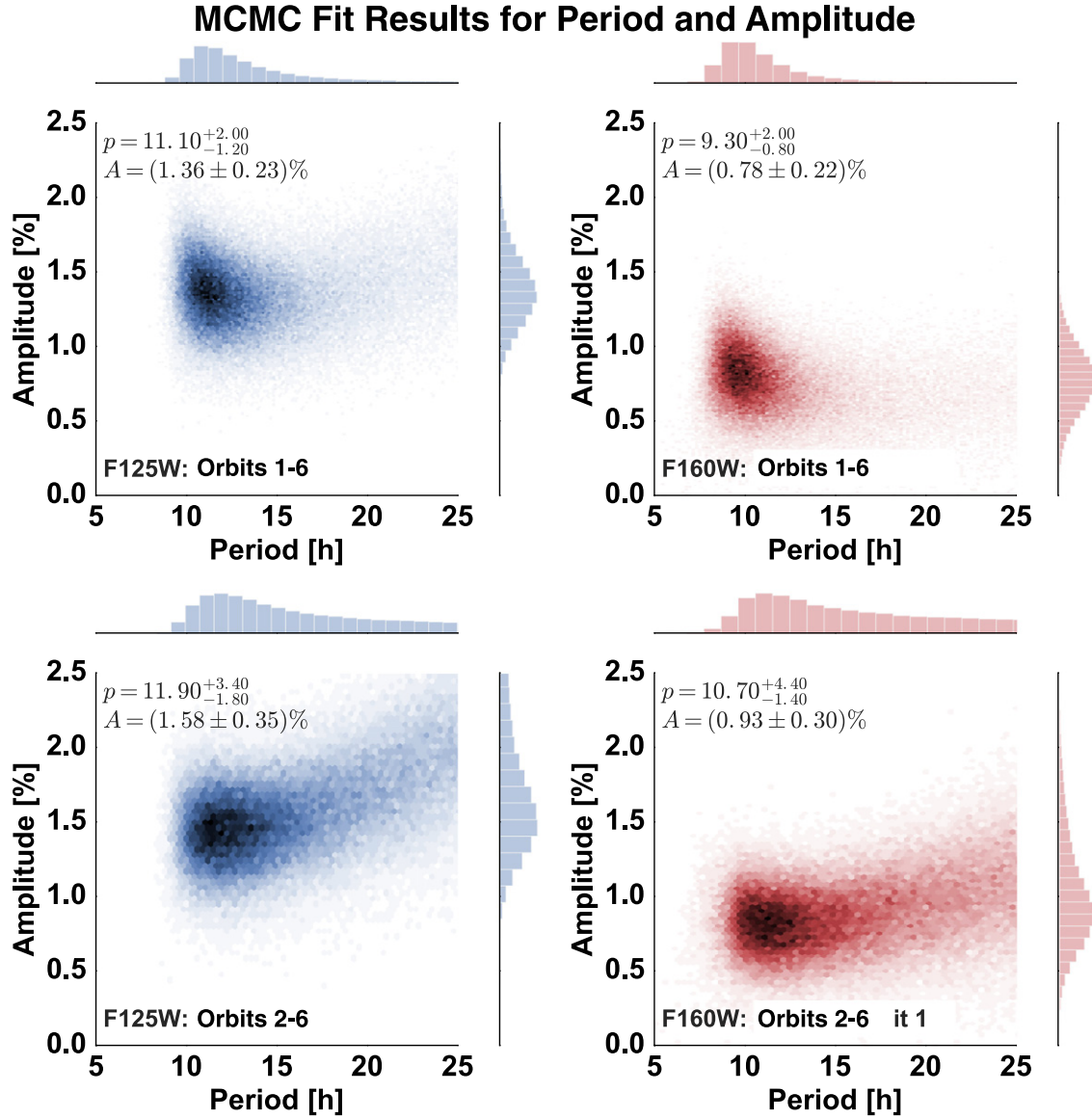
MCMC Fit Results for Period and Amplitude

Figure 4. Posterior distributions for amplitudes and periods for F125W (left) and F160W (right) light curves, using data from orbits 1–6 (upper) and data from orbits 2–6 (lower). In each panel, the univariate distributions for period and amplitude are plotted along side with the joint distribution. The values and uncertainties of period and amplitude are shown on the upper left corner of each panel.

little evidence for angular momentum loss (Bouvier et al. 2014; Scholz et al. 2015) for the first few Myr of evolution, and agree with the model of solid body rotation. In contrast, young low mass star experience strong angular momentum loss and internal angular momentum redistribution at similar ages. Rotation periods of planetary mass objects with well established age measurements can place further constraint on the gravitational contraction and angular momentum evolution in the planetary mass regime.

Our inferred rotation period is very similar to those of Jupiter and Saturn, which have periods of 9.9 and 10.5 hr, respectively. Moreover, our inferred rotation is sufficiently fast that—just as with Jupiter and Saturn—the atmospheric dynamics is likely to be rotationally dominated at regional to global scales (Showman & Kaspi 2013). The importance of rotation can be characterized by the Rossby number $Ro = U/\Omega L$, where U is the characteristic wind speed, Ω is the angular rotation rate

$(1.7 \times 10^{-4}\,\mathrm{s}^{-1}$ for a 10-hr rotation period), and L is the characteristic horizontal length scale. Showman & Kaspi (2013) presented a theory of the atmospheric circulation on brown dwarfs and directly imaged giant planets, which predicts wind speeds in the range of tens to hundreds of m s^{-1} depending on parameters. Using similar arguments, Apai et al. (2013) argued for wind speeds of a few hundreds m s^{-1} (somewhat faster than typical in Jupiter) in two L/T transition brown dwarfs. Global simulations of the atmospheric circulation using a one-layer model by Zhang & Showman (2014) predict a similar range. Considering wind speeds ranging from 10 to 1000 m s^{-1}, a circulation that is global in scale ($L = R_{\mathrm{Jup}}$) implies Rossby numbers of 0.001 to 0.1 on 2M1207b (see Figure 1 in Showman & Kaspi 2013). For a circulation whose length scale is 0.1 R_{Jup}, the Rossby numbers would range from 0.01 to 1 depending on wind speed. Thus, over almost the full range of plausible parameters, we expect that the large-scale

Table 1
F125W Photometry Results

Orbit	Pos. Angle (°)	Dither Position	T - JD$_0$ (hr)	Flux$_{prim}$ (e$^-$/s)	Flux$_{prim}$ normalized	Flux$_{comp}$ (e$^-$/s)	Flux$_{comp}$ normalized
1	202	1	0.000	76400.23	0.9842	197.47	1.0255
		1	0.030	77067.92	0.9928	194.68	1.0110
		1	0.059	77335.85	0.9963	194.17	1.0084
		2	0.192	77461.98	0.9907	192.72	0.9860
		2	0.221	77498.89	0.9912	197.69	1.0114
		2	0.251	77807.67	0.9951	194.43	0.9947
		3	0.354	76836.70	0.9896	189.01	1.0205
		3	0.384	77254.05	0.9950	188.09	1.0155
		3	0.413	77474.72	0.9978	184.35	0.9953
		4	0.546	77188.85	0.9915	182.92	0.9843
		4	0.575	77384.02	0.9940	190.81	1.0267
2	227	1	1.594	77839.67	0.9990	194.62	1.0401
		1	1.624	77952.59	1.0005	191.95	1.0258
		1	1.653	77874.77	0.9995	188.82	1.0091
		2	1.786	77221.62	0.9920	192.39	0.9974
		2	1.815	77989.91	1.0019	193.38	1.0025
		2	1.845	77810.97	0.9996	200.23	1.0380
		3	1.948	78412.56	0.9989	199.15	1.0223
		3	1.978	78506.68	1.0001	196.32	1.0077
		3	2.007	78569.23	1.0009	196.42	1.0083
		4	2.139	77237.39	0.9956	202.16	1.0228
		4	2.169	77530.01	0.9994	203.36	1.0289
3	202	1	3.188	77956.86	1.0043	191.32	0.9936
		1	3.218	78179.49	1.0072	191.70	0.9956
		1	3.247	78213.98	1.0076	195.27	1.0141
		2	3.379	78591.12	1.0051	203.01	1.0386
		2	3.409	78608.24	1.0054	197.20	1.0089
		2	3.439	78847.12	1.0084	195.33	0.9993
		3	3.542	77870.59	1.0029	184.67	0.9971
		3	3.571	78204.56	1.0072	182.92	0.9876
		3	3.601	78190.32	1.0070	185.51	1.0016
		4	3.733	77932.39	1.0010	187.29	1.0078
		4	3.763	78139.97	1.0037	186.62	1.0041
		4	3.793	78320.57	1.0060	186.88	1.0056
4	227	1	4.782	77939.05	1.0003	185.86	0.9933
		1	4.811	78127.91	1.0027	189.97	1.0153
		1	4.841	78240.98	1.0042	184.40	0.9855
		2	4.973	77857.88	1.0002	184.41	0.9560
		2	5.003	78020.08	1.0023	190.59	0.9880
		2	5.033	78140.80	1.0038	198.42	1.0286
		3	5.136	78268.69	0.9971	191.85	0.9848
		3	5.165	78559.50	1.0008	195.65	1.0043
		3	5.195	78640.39	1.0018	196.62	1.0093
		4	5.327	77340.36	0.9969	198.37	1.0037
		4	5.357	77671.12	1.0012	196.15	0.9924
		4	5.387	77871.34	1.0038	194.04	0.9818
5	202	1	6.391	77600.12	0.9997	189.87	0.9861
		1	6.421	77859.67	1.0030	188.72	0.9800
		1	6.450	77996.08	1.0048	189.82	0.9858
		2	6.582	78167.24	0.9997	195.86	1.0020
		2	6.612	78393.06	1.0026	193.02	0.9875
		2	6.642	78320.96	1.0017	189.91	0.9716
		3	6.745	77489.71	0.9980	184.65	0.9970
		3	6.774	77745.72	1.0013	183.84	0.9926
		3	6.804	77746.48	1.0013	183.86	0.9927
		4	6.936	77799.03	0.9993	181.59	0.9771
		4	6.966	77910.98	1.0007	185.86	1.0001
		4	6.996	78149.82	1.0038	184.81	0.9944

Table 1
(Continued)

Orbit	Pos. Angle (°)	Dither Position	T - JD$_0$ (hr)	Flux$_{prim}$ (e$^-$/s)	Flux$_{prim}$ normalized	Flux$_{comp}$ (e$^-$/s)	Flux$_{comp}$ normalized
		1	8.063	77432.59	0.9938	185.75	0.9927
		1	8.092	77916.03	1.0000	182.53	0.9755
		1	8.122	77916.40	1.0000	180.14	0.9627
		2	8.254	77800.14	0.9995	188.38	0.9766
		2	8.284	77805.98	0.9995	193.43	1.0028
		2	8.314	77923.23	1.0011	194.87	1.0102
6	227	3	8.417	78389.06	0.9986	194.13	0.9965
		3	8.446	78630.61	1.0017	192.12	0.9862
		3	8.476	78515.42	1.0002	191.06	0.9807
		4	8.608	77414.03	0.9979	198.44	1.0040
		4	8.638	77724.12	1.0019	194.72	0.9852
		4	8.668	77842.54	1.0034	193.93	0.9812

(This table is available in machine-readable form.)

circulation on 2M1207b—like Jupiter, Saturn, and most brown dwarfs—exhibits a Rossby number much less than one. This implies that the atmospheric circulation is rotationally dominated and that the horizontal force balance is approximately geostrophic, that is, a balance between Coriolis and pressure-gradient forces.

From the perspective of atmospheric dynamics, 2M1207b exhibits other important similarities to brown dwarfs. Its high effective temperature indicates that—like most brown dwarfs—2M1207b exhibit a strong interior heat flux presumably transported by convection, and that, by comparison, the external irradiation is negligible to the circulation. These similarities suggest that the overall dynamical mechanisms for driving an atmospheric circulation on 2M1207b should be similar to those on brown dwarfs. Thus, given the prevalence of infrared light curve variability observed on brown dwarfs, it is expected to find such variability on directly imaged planets like 2M1207b. Nevertheless, directly imaged planets generally have lower surface gravity than field brown dwarfs, and this will affect the details of the atmospheric circulation, potentially including the cloud patchiness. Further observations of 2M1207b and other directly imaged planets will help to elucidate these differences. Key questions for the future will include assessing the extent to which the atmospheric circulation on 2M1207b—including the existence of absence of zonal (east–west) jet streams, vortices, storms, and turbulence, and their effect on cloud patchiness—are similar or different than that on typical field brown dwarfs.

Our observations also allow us to compare the relative amplitudes in the J- and H-bands with the handful of brown dwarfs for which high-quality near-infrared time-resolved observations have been obtained. In the right panel of Figure 5, we compare the relative amplitude of J- and H-bands of 2M1207b and brown dwarfs (Apai et al. 2013; Buenzli et al. 2012, 2015; Yang et al. 2015) that have different spectral types and J–H colors. J and H band fluxes for brown dwarfs are integrated from WFC3 grism spectra using standard J and H filter transmission profile. We find an interesting possible correlation between the spectral types of the objects and their J-to H-band amplitude ratios. In the right panel of Figure 5, we show that earlier spectral type objects have larger amplitudes at shorter wavelength than at longer wavelengths. Interestingly, although the J–H color of 2M1207b is significantly redder, its relative amplitude ratio is very similar to that of 2M1821,

which also has an L5 spectral type (Yang et al. 2015). This exciting, but tentative trend must be confirmed with a larger sample of sources that also sample a broader range of surface gravities as well as spectral types. If the larger sample verifies the trend suggested by our small sample, the amplitude ratio will provide a powerful probe of the spectral type and surface gravity dependence of vertical cloud structure.

Recently, Karalidi et al. (2015) showed that an MCMC-optimized light curve modeling tool can correctly retrieve two-dimensional atmospheric features from high quality light curves. In the future, with higher signal-to-noise light curves of planetary mass objects and exoplanets we will be able to map their atmospheres in greater detail.

7. CONCLUSIONS

In summary, from our J- and H-band high precision, high-cadence light curves we discovered sinusoidal modulations in the planetary-mass object 2M1207b. This is the first detection of rotational modulations in a directly imaged planetary-mass object. By fitting the sinusoids to the light curves, we find a period of $10.7^{+1.2}_{-0.6}$ hr that is 20% longer than our observation baseline and should be further constrained with full phase coverage in the future. The 10.7-hr period is similar to that derived from $v \sin i$ measurements for the directly imaged exoplanet β Pic b. The period of 2M1207b is longer than most field brown dwarfs with known rotation period, but is similar to brown dwarfs in a sample with an age similar to that of 2M1207b. The amplitude ratio of J- and H-band is very similar to that of a field brown dwarf with identical L5 spectral type, although they have very different J–H colors.

Finally, we note that the observations presented here open an exciting new window on directly imaged exoplanets and planetary-mass companions. Our study demonstrates a successful application of high contrast, high-cadence, high-precision photometry with planetary mass companion. We also show that these observations can be carried out simultaneously at multiple wavelengths, allowing us to probe multiple pressure levels. With observation of a larger sample and at multiple wavelengths, we will be able to explore the detailed structures of atmospheres of directly imaged exoplanets, and identify the key parameters that determine these.

Table 2
F160W Photometry Results

Orbit	Pos. Angle (°)	Dither Position	T - JD$_0$ (hr)	Flux$_{prim}$ (e$^-$/s)	Flux$_{prim}$ normalized	Flux$_{comp}$ (e$^-$/s)	Flux$_{comp}$ normalized
1	202	1	0.091	63247.39	0.9949	309.55	0.9789
		1	0.121	63231.17	0.9947	320.57	1.0138
		1	0.150	63234.83	0.9947	310.39	0.9816
		2	0.282	62880.74	0.9899	314.73	0.9965
		2	0.312	63170.96	0.9945	319.87	1.0127
		3	0.445	63482.02	0.9909	312.57	1.0003
		3	0.474	63876.58	0.9970	314.81	1.0075
		3	0.504	63868.25	0.9969	316.42	1.0126
		4	0.607	63268.09	0.9911	305.45	0.9924
		4	0.636	63637.60	0.9969	310.09	1.0074
2	227	1	1.685	63800.82	1.0014	317.96	1.0094
		1	1.714	63646.56	0.9990	320.24	1.0167
		1	1.744	63712.52	1.0001	318.32	1.0106
		2	1.876	62867.13	0.9951	327.52	1.0173
		2	1.906	63215.33	1.0007	322.00	1.0001
		3	2.039	63472.43	0.9940	312.25	1.0059
		3	2.068	64211.58	1.0056	314.82	1.0142
		3	2.098	64018.46	1.0025	307.83	0.9917
		4	2.201	63356.87	0.9965	315.89	1.0031
		4	2.230	63173.89	0.9937	318.91	1.0127
3	202	1	3.279	63508.62	0.9991	321.56	1.0169
		1	3.308	63639.15	1.0011	321.16	1.0156
		1	3.338	63817.51	1.0039	318.01	1.0057
		2	3.470	63713.27	1.0030	317.28	1.0046
		2	3.500	63948.17	1.0067	318.58	1.0087
		3	3.632	64133.71	1.0010	318.27	1.0185
		3	3.662	64148.99	1.0013	316.10	1.0116
		3	3.692	64378.74	1.0049	310.91	0.9950
		4	3.824	64067.16	1.0036	300.93	0.9777
		4	3.854	64067.97	1.0036	308.13	1.0011
		4	3.884	63910.80	1.0011	314.97	1.0233
4	227	1	4.872	63914.07	1.0032	311.23	0.9880
		1	4.902	63884.46	1.0028	315.39	1.0013
		1	4.932	63920.45	1.0033	314.80	0.9994
		2	5.064	63364.21	1.0030	321.69	0.9992
		2	5.094	62992.57	0.9971	320.14	0.9944
		3	5.226	63789.12	0.9990	310.93	1.0017
		3	5.256	64018.91	1.0025	312.98	1.0083
		3	5.286	63849.69	0.9999	309.99	0.9986
		4	5.418	63722.64	1.0023	316.11	1.0038
		4	5.448	63707.71	1.0021	312.25	0.9915
		4	5.477	63813.00	1.0037	314.67	0.9992
5	202	1	6.482	63771.50	1.0032	306.82	0.9703
		1	6.511	63910.88	1.0054	316.82	1.0019
		1	6.541	63759.91	1.0030	321.02	1.0152
		2	6.673	63587.56	1.0011	315.41	0.9986
		2	6.703	63817.91	1.0047	309.17	0.9789
		3	6.836	64135.94	1.0011	303.13	0.9701
		3	6.865	64302.83	1.0037	306.83	0.9819
		3	6.895	64273.25	1.0032	313.31	1.0027
		4	7.027	64005.66	1.0026	304.82	0.9903
		4	7.057	63728.45	0.9983	307.86	1.0002
		4	7.087	64020.34	1.0029	310.13	1.0076
6	227	1	8.154	63248.40	0.9928	314.61	0.9988
		1	8.183	63573.69	0.9979	309.55	0.9827
		1	8.213	63681.11	0.9996	312.85	0.9932
		2	8.345	63367.46	1.0031	317.65	0.9866
		2	8.375	63238.70	1.0010	322.75	1.0025
		3	8.508	63746.16	0.9983	306.08	0.9861

Table 2
(Continued)

Orbit	Pos. Angle (°)	Dither Position	T - JD$_0$ (hr)	Flux$_{prim}$ (e$^-$/s)	Flux$_{prim}$ normalized	Flux$_{comp}$ (e$^-$/s)	Flux$_{comp}$ normalized
		3	8.537	63724.29	0.9979	309.73	0.9978
		3	8.567	63874.72	1.0003	309.08	0.9957
		4	8.699	63614.87	1.0006	309.17	0.9817
		4	8.729	63530.79	0.9993	320.22	1.0168
		4	8.759	63696.84	1.0019	312.14	0.9912

(This table is available in machine-readable form.)
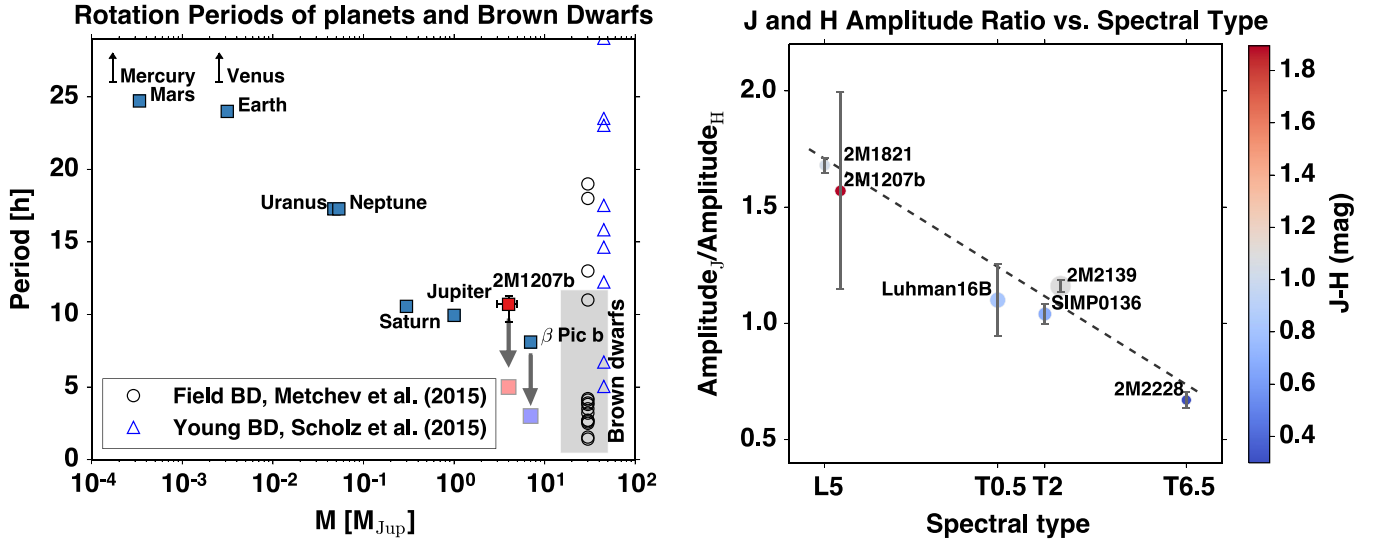
Figure 5. Comparison of 2M1207's rotation period and color change with brown dwarfs, β Pic b, and solar system planets. Left: period vs. mass plot for 2M1207b (red square), solar system planets and β Pic b (blue squares), field brown dwarfs from the study of Metchev et al. (2015) (black circles, gray shade) and young brown dwarfs from the study of Scholz et al. (2015) (blue triangles). Final rotation rates for 2M1207b and β Pic b estimated based on conservation of angular momentum are plotted with faint red and blue squares, respectively. The mass of brown dwarfs are assumed to be $\sim$30 M_{Jup}, and the difference mass of field brown dwarfs and young brown dwarfs are added artificially for the sake of clarity. The gray rectangle that has a $\pm$15 M_{Jup} range in x, and a $\pm\sigma$ of field brown dwarf periods range in y, indicates a region where field brown dwarfs most likely to appear in this diagram. Rotation period monotonically decreases with the increase of mass. Right: ratio of modulation amplitude in J and H band vs. spectral type for 2M1207b and brown dwarfs. The point for 2M1207b is shifted to $+x$ for half spectral type for clarification. The colors of the points represent J$-$H magnitude, and the sizes of the points are proportional to the J-band modulation amplitudes. The gray dashed line is the result of a linear fit to these points. Correlation of J- and H-band modulation amplitude ratio and spectral type is shown.

REFERENCES

Ackerman, A. S., & Marley, M. S. 2001, ApJ, 556, 872
Allard, F., Homeier, D., & Freytag, B. 2012, RSPTA, 370, 2765
Apai, D., Radigan, J., Buenzli, E., et al. 2013, ApJ, 768, 121
Baraffe, I., Chabrier, G., Barman, T. S., Allard, F., & Hauschildt, P. H. 2003, A&A, 402, 701
Barman, T. S., Macintosh, B., Konopacky, Q. M., & Marois, C. 2011, ApJL, 735, L39
Berta, Z. K., Charbonneau, D., Désert, J.-M., et al. 2012, ApJ, 747, 35

Biller, B. A., Vos, J., Bonavita, M., et al. 2015, ApJL, 813, 23
Biretta, J. 2014, wfc rept, 1, 10
Bonnefoy, M., Chauvin, G., Lagrange, A.-M., et al. 2014, A&A, 562, A127
Bouvier, J., Matt, S. P., Mohanty, S., et al. 2014, in Protostars and Planets VI, Vol. 1; Angular Momentum Evolution of Young Low-Mass Stars and Brown Dwarfs: Observations and Theory, ed. H. Beuther, R. S. Klessen, C. P. Dullemond & T. Henning (Tucson, AZ: Univ. Arizona Press), 433
Buenzli, E., Apai, D., Morley, C. V., et al. 2012, ApJL, 760, L31
Buenzli, E., Saumon, D., Marley, M. S., et al. 2015, ApJ, 798, 127
Burgasser, A. J., Sheppard, S. S., & Luhman, K. L. 2013, ApJ, 772, 129
Burrows, A., Sudarsky, D., & Hubeny, I. 2006, ApJ, 640, 1063
Chauvin, G., Lagrange, A.-M., Dumas, C., et al. 2004, A&A, 425, L29
Chauvin, G., Lagrange, A.-M., Dumas, C., et al. 2005a, A&A, 438, L25
Chauvin, G., Lagrange, A.-M., Zuckerman, B., et al. 2005b, A&A, 438, L29
Currie, T., Burrows, A., Itoh, Y., et al. 2011, ApJ, 729, 128
Dressel, L. 2012, Wide Field Camera 3, HST Instrument Handbook, Vol. 1
Ducourant, C., Teixeira, R., Chauvin, G., et al. 2008, A&A, 477, L1
Heinze, A. N., Metchev, S., & Kellogg, K. 2015, ApJ, 801, 104
Helling, C., Ackerman, A., Allard, F., et al. 2008, MNRAS, 391, 1854
Karalidi, T., Apai, D., Schneider, G., Hanson, J. R., & Pasachoff, J. M. 2015, ApJ, 814, 65
Klein, R., Apai, D., Pascucci, I., Henning, T., & Waters, L. B. F. M. 2003, ApJL, 593, L57
Kostov, V., & Apai, D. 2013, ApJ, 762, 47
Kreidberg, L., Bean, J. L., Désert, J.-M., et al. 2014, Natur, 505, 69
Krist, J. 1995, adass IV, 77, 349

Lallo, M., Makidon, R. B., Casertano, S., Gilliland, R., & Stys, J. 2005, HST Temporal Optical Behavior and Current Focus Status, Tech. rep, 3

Lodato, G., Delgado-Donate, E., & Clarke, C. J. 2005, MNRAS Lett, 364, L91

MacKenty, J. W., Kimble, R. A., O'Connell, R. W., & Townsend, J. A. 2008, Proc. SPIE, 7010, 1

Madhusudhan, N., Burrows, A., & Currie, T. 2011, ApJ, 737, 34

Mandell, A. M., Haynes, K., Sinukoff, E., et al. 2013, ApJ, 779, 128

Marley, M. S., Saumon, D., Cushing, M., et al. 2012, ApJ, 754, 135

Marley, M. S., Saumon, D., & Goldblatt, C. 2010, ApJL, 723, L117

Marley, M. S., & Sengupta, S. 2011, MNRAS, 417, 2874

Marois, C., Macintosh, B., Barman, T., et al. 2008, Sci, 322, 1348

Marois, C., Zuckerman, B., Konopacky, Q. M., Macintosh, B., & Barman, T. 2010, Natur, 468, 1080

Metchev, S. A., Heinze, A., Apai, D., et al. 2015, ApJ, 799, 154

Mohanty, S., Greaves, J., Mortlock, D., et al. 2013, ApJ, 773, 168

Mohanty, S., Jayawardhana, R., Huelamo, N., & Mamajek, E. 2007, ApJ, 657, 1064

Patience, J., King, R. R., De Rosa, R. J., & Marois, C. 2010, AA, 517, A76

Radigan, J., Jayawardhana, R., Lafrenière, D., et al. 2012, ApJ, 750, 105

Reiners, A., & Basri, G. 2008, ApJ, 684, 1390

Scholz, A., Kostov, V., Jayawardhana, R., & Mužić, K. 2015, ApJ, 809, L29

Showman, A. P., & Kaspi, Y. 2013, ApJ, 776, 85

Skemer, A. J., Close, L. M., Szűcs, L., et al. 2011, ApJ, 732, 107

Skemer, A. J., Hinz, P. M., Esposito, S., Burrows, A., et al. 2012, ApJ, 753, 14

Snellen, I. A. G., Brandl, B. R., de Kok, R. J., et al. 2014, Natur, 509, 63

Song, I., Schneider, G., Zuckerman, B., et al. 2006, ApJ, 652, 724

Sterzik, M. F., Pascucci, I., Apai, D., van der Bliek, N., & Dullemond, C. P. 2004, A&A, 427, 245

Yang, H., Apai, D., Marley, M. S., et al. 2015, ApJL, 798, L13

Zhang, X., & Showman, A. P. 2014, ApJL, 788, L6